Implicit Large Eddy Simulation and Attempts to Supersonic Combustion

By W. Wei, B. Wang, AND X. Hu†

School of Aerospace, Tsinghua University, 100084 Beijing, China
†Lehrstuhl für Aerodynamik und Strömungsmechanik, TU München Germany

The study of implicit large eddy simulation and its application to supersonic combustion was conducted. Three different shock-capturing schemes were used to calculate the convective flux, and a sixth-order compact one for the viscous flux. Taylor-Green vortex (TGV) problem was taken as the benchmark case and the changing of total kinetic energy and energy spectrum was analyzed. TGV with passive scalar mixing and reaction was also simulated. Scalar variances in different Schmidt numbers and different grids were compared and analyzed. The reaction rate and diffusivity were modified to deal with the chemical reaction source term, and the comparison of reaction rate PDF and flame structure was given. ILES was then successfully applied in the supersonic mixing layer flow and the statistical results consists well with the experimental data. The combustion case in the mixing layer flow was also realized although the reaction rate model in ILES has not well been resolved.

1. Introduction

Direct numerical simulation can resolve all scales of flow field, and it can give us all the fluctuation information. However, it costs too much computing resource with high Re number. RANS and LES are often adopted as an alternative [1–3]. But they have the same disadvantage that empirical coefficients are used to close the simulation model and they are not universal for all flows.

Recently, a lot of studies on implicit large eddy simulation are carried out. This method solves the Navier-Stokes equations directly, and don't need to model the subgrid stress. But it is not robust, since it can't guarantee that implicit dissipation equals to physical dissipation. It has high requirements on the numerical scheme, and the shock-capturing method would be a good choice [4]. Since it can eliminate numerical oscillations, which has the similar function of grid filtering in LES. If the scheme dissipation can be taken as the efficient viscosity of Sub-Grid-Scale, an implicit LES is realized practically.

A lot of shock-capturing schemes have been developed since Jay P. Boris proposed the original idea of "capturing physics with numerics" on the basis of the Flux-Corrected Transport (FCT) convection algorithm in 1970s. In this study, we will use three different shock-capturing schemes to establish the implicit large eddy simulation and compare the results with each other (the details of these schemes will be given in part 2).

Until now, the implicit large eddy simulation has been successfully applied in isotropic turbulence, wall bounded and jet flows [5–7]. However, seldom studies have extended its application into combustion. In this paper, we will try to employ the implicit large eddy simulation to simulate the three-dimensional supersonic reacting mixing layer.

2. Numerical Method

2.1. *Governing equations*

The unsteady compressible Navier-Stokes equations considering reaction without body force used in the present study read as,

$$\frac{\partial \rho}{\partial t} + \frac{\partial \rho u_j}{\partial x_j} = 0 \tag{2.1}$$

$$\frac{\partial \rho u_i}{\partial t} + \frac{\partial (\rho u_i u_j + p\delta_{ij})}{\partial x_j} = \frac{\partial \tau_{ij}}{\partial x_j} \tag{2.2}$$

$$\frac{\partial \rho E}{\partial t} + \frac{\partial (\rho E + p)u_j}{\partial x_j} = \frac{\partial \tau_{ij}u_i}{\partial x_j} + \frac{\partial q_j}{\partial x_j} \tag{2.3}$$

$$\frac{\partial \rho Y_k}{\partial t} + \frac{\partial \rho Y_k u_j}{\partial x_j} = \frac{\partial}{\partial x_j}(\rho D_k \frac{\partial Y_k}{\partial x_j}) + \dot{\omega}_k \tag{2.4}$$

$$\dot{\omega}_k = W_k \sum_{j=1}^{M} v_{kj} Q_j \tag{2.5}$$

In order to close the above equations, the state equation should be added as follows

$$p = \rho RT \tag{2.6}$$

where ρ, p, Y_k and u_i denote the fluid density, pressure, the mass fraction of species k and the velocity components in the ith direction, respectively. Here,

$$\tau_{ij} = \mu(\frac{\partial u_i}{\partial x_j} + \frac{\partial u_j}{\partial x_i} - \frac{2}{3}\frac{\partial u_k}{\partial x_k}\delta_{ij}) \tag{2.7}$$

is the viscous stress;

$$q_j = -\lambda\frac{\partial T}{\partial x_j} + \sum_k \rho h_k D_k \frac{\partial Y_k}{\partial x_j} \tag{2.8}$$

is the heat flux;

$$E = e + \frac{1}{2}u_j u_j + h_f \tag{2.9}$$

is the total energy. Here,

$$e = \int_{T_0}^{T} c_v \mathrm{d}T \tag{2.10}$$

is the internal energy;

$$h_f = \sum_k Y_k h_{f,k} \tag{2.11}$$

is the standard enthalpy of formation.

μ, λ and D_k denote the molecular viscosity, the thermal conductivity and the diffusion coefficient of species k respectively. $\dot{\omega}_k$ is the rate of production of species k; W_k is the molecular weight of species k; ν_{kj} is the coefficient of species k in the jth reaction; Q_j is the rate of the jth reaction.

2.2. *Discretization method*

The viscous terms of above governing equations are computed using the sixth-order symmetric compact difference scheme,

$$\frac{1}{3}\hat{F}_{j+1} = \frac{28\left(\hat{f}_{j+1} - \hat{f}_{j-1}\right) + \left(\hat{f}_{j+2} - \hat{f}_{j-2}\right)}{36\Delta x} \tag{2.12}$$

where $\hat{F}_j$ is the difference approximation for $\left(\frac{\partial \hat{f}}{\partial x}\right)_j$ at the node j.

The time integration uses the third-order explicit Runge-Kutta scheme. For example, for a semi-discrete equation of $\frac{dU_j}{dt} = L_j(U)$, the iteration from n to iteration $n+1$ is performed as,

$$U_j^{(1)} = U_j^n + \Delta t L_j\left(U^n\right)$$
$$U_j^{(2)} = \frac{3}{4}U_j^n + \frac{1}{4}U_j^{(1)} + \frac{1}{4}\Delta t L_j\left(U_j^{(1)}\right) \tag{2.13}$$
$$U_j^{n+1} = \frac{1}{3}U_j^n + \frac{2}{3}U_j^{(2)} + \frac{2}{3}\Delta t L_j\left(U_j^{(2)}\right)$$

where U_j was the conserved variable at the direction j.

Then we focus on the discrete method of convection terms, which is very important for numerical stability. Here we use three different numerical schemes, upwind WENO, WENO-CU, and WENO-LU respectively.

2.2.1. *WENO scheme*

The fifth-order upwind weighted essentially non-oscillatory (WENO) scheme proposed by Jiang [8] in 1996 is adopted in this paper. Here we briefly give the formation in the context of the one-dimensional advection equation.

$$\frac{\partial u}{\partial t} + \frac{\partial f(u)}{\partial x} = 0 \tag{2.14}$$

The flux $f_{j+1/2}^{WENO}$, for the interface at $j + 1/2$, is evaluated using the values of five points, which are $j-2$, $j-1$, j, $j+1$, and $j+2$. It is the combination of three numerical fluxes calculated in the correspond stencils,

$$f_{j+1/2}^{WENO} = \sum_{k=1}^{3} \omega_k f_{j+1/2}^k \tag{2.15}$$

Here the fluxes are

$$f_{j+1/2}^{(1)} = \frac{1}{3}f_{j-2} - \frac{7}{6}f_{j-1} + \frac{11}{6}f_j \tag{2.16}$$

$$f_{j+1/2}^{(2)} = -\frac{1}{6}f_{j-1} + \frac{5}{6}f_j + \frac{1}{3}f_{j+1} \tag{2.17}$$

$$f_{j+1/2}^{(3)} = \frac{1}{3}f_j + \frac{5}{6}f_{j+1} - \frac{1}{6}f_{j+2} \tag{2.18}$$

And the weights ω_k are

$$\omega_k = \frac{\alpha_k}{\alpha_1 + \alpha_2 + \alpha_3} , \alpha_k = \frac{C_k}{(\varepsilon + IS_k)^p} \tag{2.19}$$

Where ε is a small positive number, and $C_1 = 1/10, C_2 = 6/10, C_3 = 3/10$,

$$IS_1 = \frac{1}{4}(f_{j-2} - 4f_{j-1} + 3f_j)^2 + \frac{13}{12}(f_{j-2} - 2f_{j-1} + f_j)^2 \tag{2.20}$$

$$IS_2 = \frac{1}{4}(f_{j-1} - f_{j+1})^2 + \frac{13}{12}(f_{j-1} - 2f_j + f_{j+1})^2 \tag{2.21}$$

$$IS_3 = \frac{1}{4}(3f_j - 4f_{j+1} + f_{j+2})^2 + \frac{13}{12}(f_j - 2f_{j+1} + f_{j+2})^2 \tag{2.22}$$

2.2.2. *WENO-CU scheme*

The WENO-CU scheme is a fifth-order hybrid scheme of WENO and compact scheme proposed by Ren [9]. It uses the WENO scheme near the discontinuity to capture shock and eliminate pseudo numerical oscillation, and the compact scheme in the smooth area to reduce dissipation. The numerical flux of the hybrid scheme is calculated as,

$$\hat{f}_{j+1/2} = \sigma_{j+1/2}\hat{f}_{j+1/2}^{CU} + \left(1 + \sigma_{j+1/2}\right)\hat{f}_{j+1/2}^{WENO} \tag{2.23}$$

which is constructed by hybridizing a fifth-order Compact Upwind (CU) scheme $\hat{f}_{j+1/2}^{CU}$ and a fifth-order WENO one $\hat{f}_{j+1/2}^{WENO}$ through a smoothness indicator r_c. $\sigma_{j+1/2}$ is the weight of the numerical fluxes,

$$\sigma_{j+1/2} = \min\left(1, \frac{r_{j+1/2}}{r_c}\right) \tag{2.24}$$

2.2.3. *WENO-LU scheme*

The WENO-LU scheme proposed by Hu [10] is also a hybrid scheme. And its idea is the same as the WENO-CU scheme, but it uses the linear upwind scheme rather than compact scheme in the smooth area, which can reduce computing time efficiently. Supposed U is the conservative variable, the flux in a certain direction $\partial F/\partial x$ is computed as an example and flux in other directions can be computed similarly.

$$\frac{\partial F}{\partial x} = \frac{1}{\Delta x}(F_{i+1/2,j} - F_{i-1/2,j}) \tag{2.25}$$

(1) The estimated value of $U_{i+1/2}$ is computed by averaging U_i and U_{i+1}, then $A = \partial F/\partial U$ at the $i + 1/2$ point is obtained.

(2) Compute the left eigenvectors of A as l_k (k is the number of solution variables) and the right eigenvectors as r_k. Calculate the eigenvalues of A, denoted as λ_k.

(3) Compute $F_{i+1/2}$ and $\Delta U_{i+1/2}$ respectively

$$F_{i+1/2} = \frac{1}{60}(F_{i-2} - 8F_{i-1} + 37F_i + 37F_{i+1} - 8F_{i+2} + F_{i+3}) \tag{2.26}$$

$$\Delta U_{i+1/2} = \frac{1}{60}(U_{i-2} - 5U_{i-1} + 10U_i - 10U_{i+1} + 5U_{i+2} - U_{i+3}) \tag{2.27}$$

(4) In the characteristic space, compute

$$\Delta v_{i+1/2,k} = l_k \cdot \Delta U_{i+1/2}, g_{i+1/2,k} = l_k \cdot F_{i+1/2} \tag{2.28}$$

Compute $\sigma_k = \left(\Delta v_{i+1/2,k}/\tilde{\rho}\right)^2$ as the dimensionless detector to measure the smoothness of the flow field, where $\tilde{\rho}$ is the average density computed.

If $\sigma_k < \varepsilon$, then

$$f_{i+1/2,k} = g_{i+1/2,k} + |\lambda_k| \Delta v_{i+1/2,k} \tag{2.29}$$

Otherwise $f_{i+1/2,s} = \tilde{f}_{i+1/2}(WENO)$, that is the flux computed using the fifth-order upwind WENO scheme.

(5) Project the numerical flux into the physical space
$\mathbf{F}_{i+1/2} = \mathbf{r} \cdot \mathbf{f}_{i+1/2}$, that is the numerical flux of $\partial \mathbf{F}/\partial x$.

3. Results and discussion

3.1. *Taylor-Green vortex (TGV) test*

According to Drikakis [11], there are two criteria to access a scheme whether it's suitable for ILES: (1) It should capture the $-5/3$ slope of the energy spectrum in the inertial sub-range; (2) It should have the ability to simulate the transition from laminar to turbulence. In this sense, the Taylor-Green vortex problem would be an idea test since it contains the stages of laminar, transition, and finally turbulence as the time develops.

The three-dimensional Taylor-Green vortex (TGV) was firstly introduced by Taylor and Green [12]. Since then, a lot of studies have been done in the TGV problem. Brachet et al. [13] did the simulation of both invicid and viscous TGV on 32^3, 64^3, 128^3 and 256^3 grids respectively. Shu et al. [14] did the inviscid TGV simulations using both the fifth-order WENO scheme and Fourier spectral methods.

In this study, we firstly did the simulations of TGV in different Re number and different grids using the above three schemes, as to access the performance of these schemes in the ILES simulation.

The computing domain is $[0, 2\pi] \times [0, 2\pi] \times [0, 2\pi]$ and the initial condition is given as below,

$$
\begin{aligned}
u &= U_0 \sin x \cos y \sin z \\
v &= -U_0 \cos x \sin y \sin z \\
w &= 0 \\
p &= p_0 + \frac{\rho_0 U_0^2}{16}(\cos 2z + 2)(cos2x + cos2y)
\end{aligned}
\tag{3.1}
$$

Set $p_0 = 100$, $\rho_0 = 1$, $U_0 = 1$, then the Mach number is about 0.08 and the flow is nearly incompressible. The boundary conditions in the three dimension are all periodic.

Figure. 1 shows the results of the total kinetic energy integrated in the entire flow field . For Re =30,000, at the beginning, the kinetic energy damps very slow and it has almost no change in the first seconds. But when the time is about 4s, the subgrid-scales are produced and the kinetic energy begins to decay due to the numerical dissipation, which also can be taken as the implicit subgrid dissipation. The results of Re number equal to 3,000 are similar, since in both the two cases, the numerical viscosity is large compared to the physical viscosity. While In the results of Re=300, there is only slight difference between the curve of WENO-LU and WENO-CU since in this case the physical viscosity is dominate. But the WENO scheme is still too dissipated.

Figure. 2 shows the contours of q criterion equal to 0.1 changing with time using WENO-LU scheme for Re=3000. As we can see, it occurs the vortex stretch firstly and the energy from the large scale is transferred to the small scale. And finally the field becomes into the isotropic turbulence. Figure. 3 gives the velocity distribution for Re=3000 in the line of $y = 0, z = \pi/2$. As we can see, firstly the curve of velocity is smooth. But
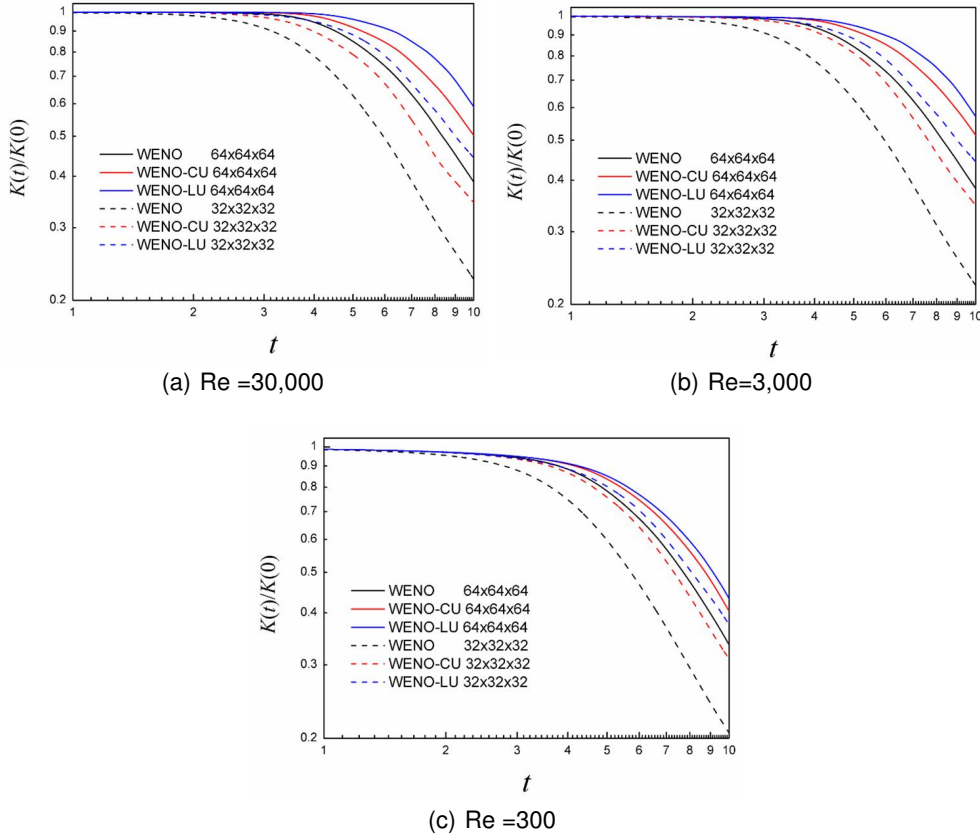
(a) Re =30,000

(b) Re=3,000

(c) Re =300

FIGURE 1. Comparison of the total kinetic energy.

as the turbulence develops, the velocity is not smooth yet and there are steep sharps which causes the kinetic energy damps rapidly.

Figure. 4 shows the energy spectrum. As the time develops, the slope of energy spectrum is also changing. And for time lager than 4, the turbulence develops and the kinetic energy builds up an inertial range. The slope is approximately $-5/3$. It implies that it can predict the characteristics of turbulence.

3.2. *TGV with passive scalar mixing*

The passive scalar transportation is very important, especially in the chemical reacting process. We solved the conserved passive scalar transport equation,

$$\frac{\partial \rho f}{\partial t} + \nabla \cdot (\rho f \vec{U}) = \nabla \cdot (\rho D \nabla f) \tag{3.2}$$

Here only the WENO-LU scheme is used since it has less dissipation and costs less computing time. The initial distribution for f is a function of the initial q distribution.

$$f(t=0) = \frac{1 + \text{erf}(C_0 Q)}{2}, C_0 = 100 \tag{3.3}$$

Here erf is the error function. Figure. 5 shows the initial f distribution. In most of regions, f equals to 1 or 0 and there is large gradient of f initially.
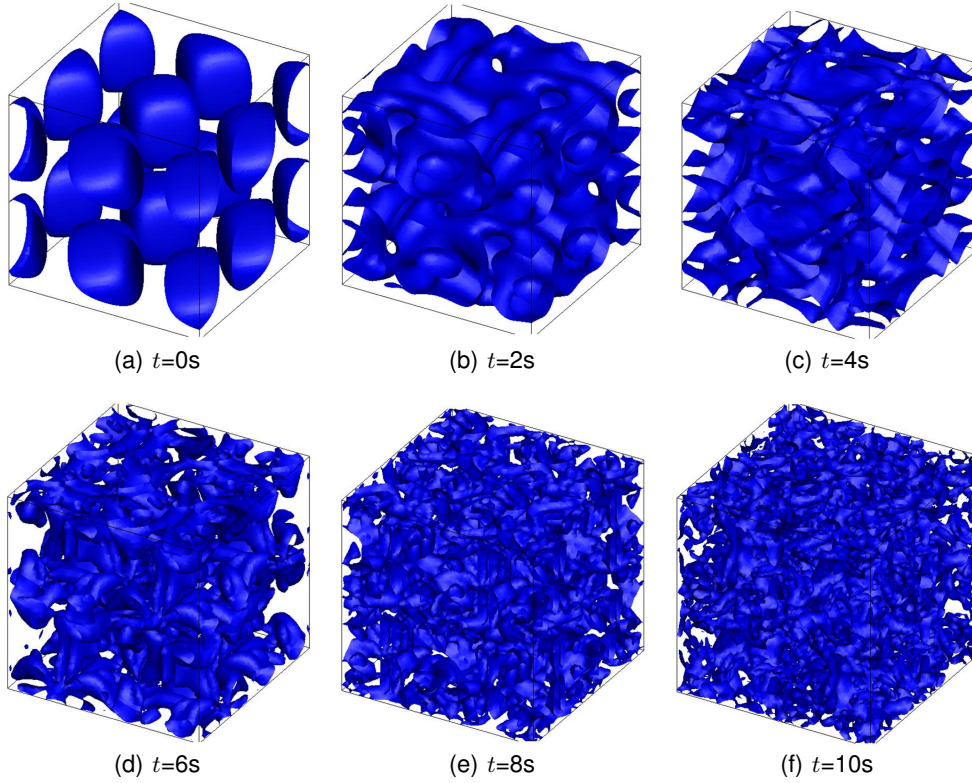
(a) t=0s   (b) t=2s   (c) t=4s

(d) t=6s   (e) t=8s   (f) t=10s

FIGURE 2. Contours of q criterion equal to 0.1 for Re=3000.

Figure. 6 shows the scalar variance curve changing with time for Re=30,000 for different Schmit numbers and in different grid resolutions. Similar to the kinetic energy, in the first 4 seconds, it occurs laminar mixing. But the dissipation is also significant due to the initial large gradient of passive scalar. For time large than 4, the turbulent mixing occurs and the dissipation of scalar variance is larger than that in laminar mixing.

Figure. 7 shows the scalar field for Re=30,000, Sc=1.0 in the plane of $z = \pi$. During the stage of laminar mixing , the interface between the high and low f region is clear and regular while in the stage of turbulent mixing, the interface is twisted, which enhances the mixing process.

3.3. *TGV with reaction*

Further, a theoretic model of TGV considering chemical reacting is studied. For simplicity, the combustion of diluted hydrogen and air is considered. The component of fuel is $0.03H_2+0.97N_2$, while the component of oxidant is $0.24O_2+0.76N_2$. The initial species distribution is given as

$$Y_i = fY_i^{fuel} + (1-f)Y_i^{ox}, f(t=0) = \frac{1 + \operatorname{erf}(C_0Q)}{2} \qquad (3.4)$$

A one-step reaction is adopted as the chemistry.

$$2H_2 + O_2 \rightarrow 2H_2O$$

(a) t=0s   (b) t=2s   (c) t=4s

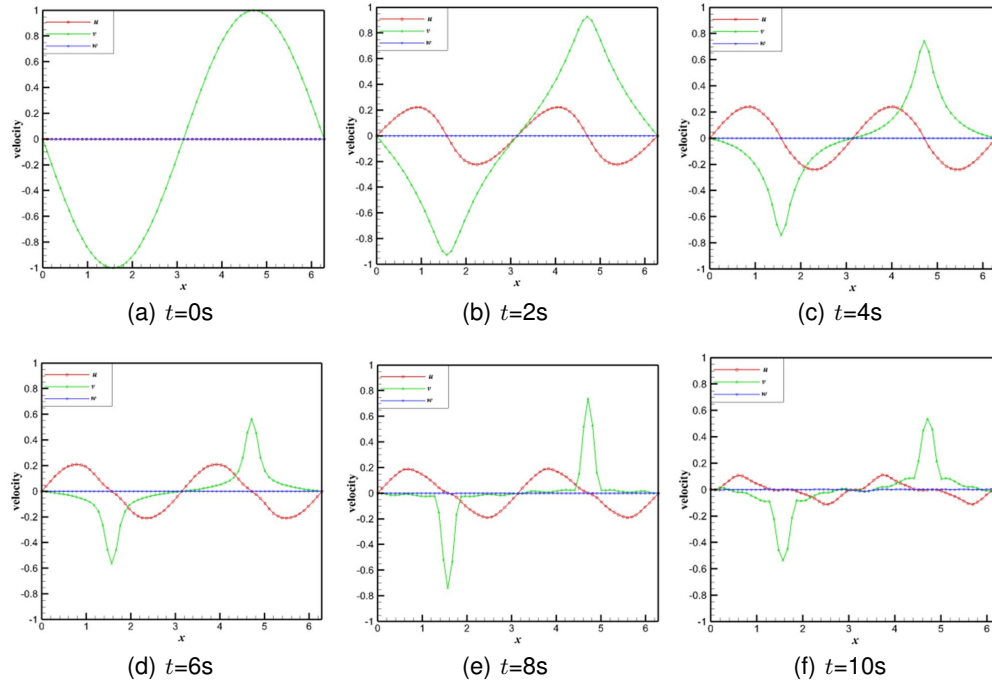(d) t=6s   (e) t=8s   (f) t=10s
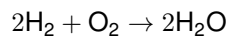
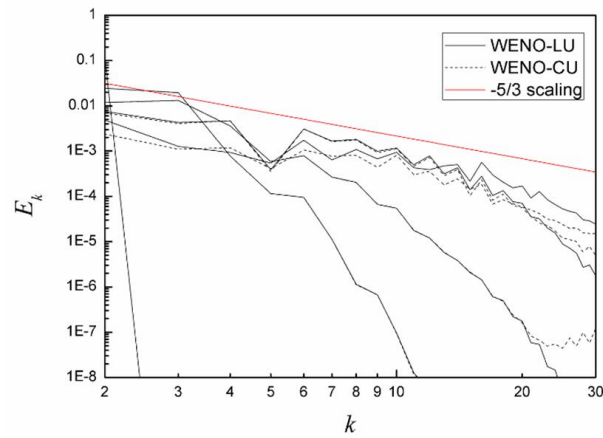FIGURE 3. The velocity distribution for Re=3000 in the line of $y = 0, z = \pi/2$.

FIGURE 4. Energy spectrum.

The reaction rate is calculated as

$$k = A \exp(-E_a/RT)[\text{H}_2]^2[\text{O}_2] \tag{3.5}$$

Where A = 9.87E16, E_a = 19824.

The problem would arise in the reacting case is that the combustion is also a strong nonlinear process. If the reacting rates are calculated using the values of temperature and species concentrations in the ILES grid, it would bring some simulation errors. To access these errors, we adopted three different methods to deal with the chemical source
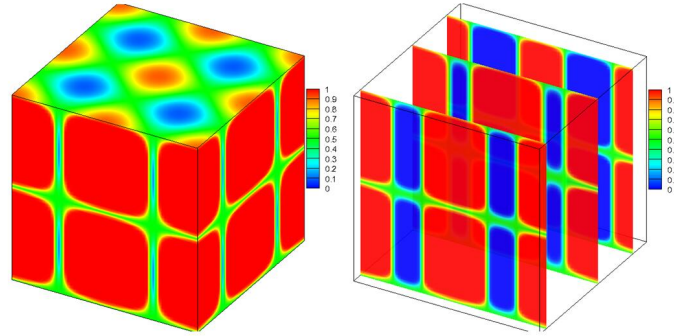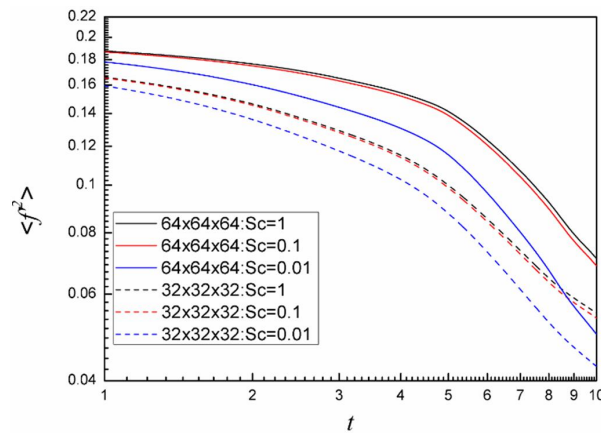
FIGURE 5. Initial f distribution.
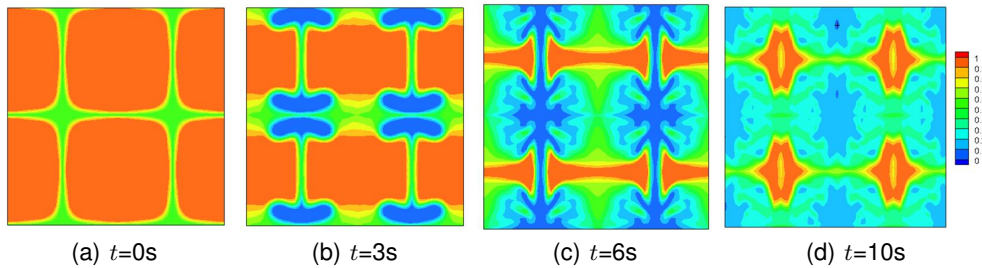

FIGURE 6. scalar variance curves.

(a) $t=0$s   (b) $t=3$s   (c) $t=6$s   (d) $t=10$s

FIGURE 7. Scalar field in the plane of $z = \pi$.

term as in Tab. 1. The first method is to calculate the mean reaction rate using the mean value of species and temperature. In the second method, we introduce the thickening factor F which modifies the diffusivity and the pre-exp factor. In the third method, we also introduce the wrinkling factor. The idea comes from the thickened flame model and details can refer to Colin's paper in 2000 [15].

Figure. 8 shows the PDF of reaction rate using different models. The results are similar with only a slight difference. Figure. 9 shows the flame structure of temperature via mixture fraction. It can be seen that close to the stoimetric point, all of the above models

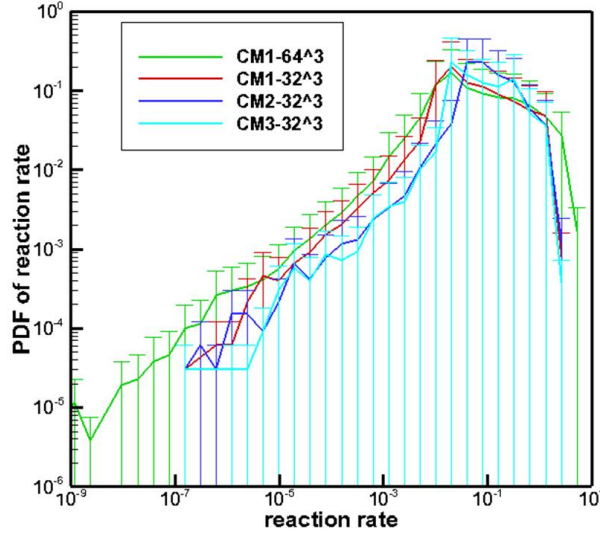|	diffusivity	pre-exp factor	case
Thin flame laminar	D	A	CM1
Thick flame laminar	FD	A/F	CM2
Thick flame turbulent	EFD	EA/F	CM3

TABLE 1. Three methods to treat the chemical source term.

FIGURE 8. Comparison of PDF of the reaction rate using different models.

predict well. Except CM3, the results of CM1 and CM2 using 32 grids are similar with CM1 using 64 grids.

3.4. *ILES of supersonic mixing layer flow*

The schematic of the supersonic mixing layer and flow parameters are shown in Fig. 10. The average velocity profile in the streamwise direction is hyperbolic tangent, and average velocity in other directions is set to zero.

$$\bar{u} = \frac{u_1 + u_2}{2} + \frac{u_1 - u_2}{2} \tanh(\frac{y - 0.5l_y}{2\delta_0}) \tag{3.6}$$

In order to stimulate the flow instability, the inlet velocity perturbation is given as

$$v' = (u_1 - u_2)G(y - 0.5l_y)A\sin(2\pi ft + \xi) \tag{3.7}$$

The flow parameters is set the same as the experiment done by Goebel et al [16]. Figure. 11 gives the simulation results of velocity moments compared with the experimental data. The statistics consists well with the experiment, which confirms the validity of ILES method applied in the supersonic mixing layer flow.

Then we conduct the reactive mixing layer flow. The fuel is still the diluted H_2, and the oxidation is air. They have the same pressure, but different temperature and velocity,
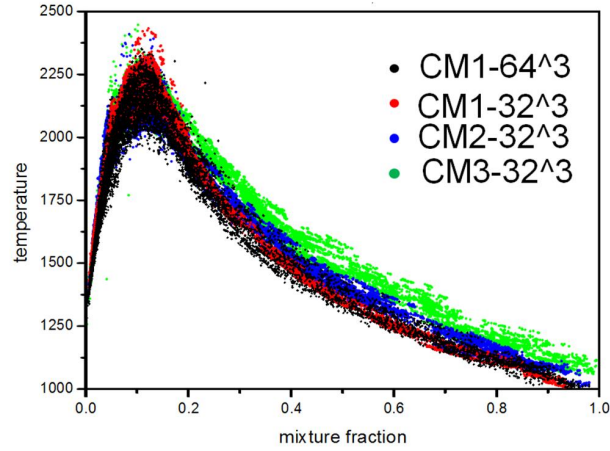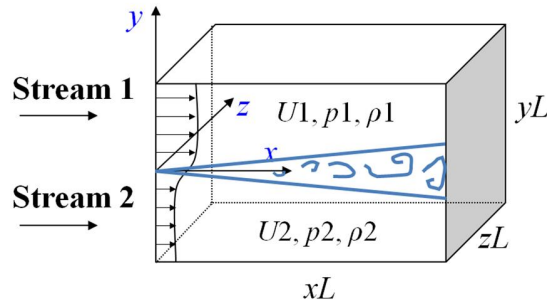
FIGURE 9. Comparison of flame structure.

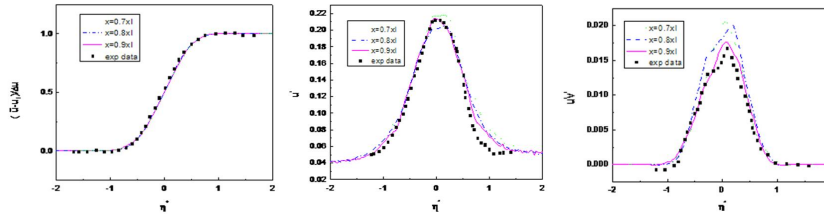FIGURE 10. Schematic of supersonic mixing layer.


FIGURE 11. Self-similarity of velocity moments.

shown in Tab. 2. Figure. 12 shows the instantaneous results of mass fraction of O_2, H_2 and temperature.

4. Conclusion and outlooks

In this study, we attempted to apply the implicit large eddy simulation into simulations of supersonic reacting flows. We chose three high-order low dissipation schemes and examine their performance employed in ILES using TGV theoretical model. Then, we tried to modify the models of reaction rate and couple them in the ILES, and evaluate the numerical results through comparing flame structure and reaction rate PDFs.

Components	Temperature(K)	Pressure(MPa)	Ma	Velocity(m/s)
$0.3H_2+0.7N_2$	390	0.1	1.13	1000
air	1100	0.1	3.0	2000

TABLE 2. Inlet conditions of reactive mixing layer flow.
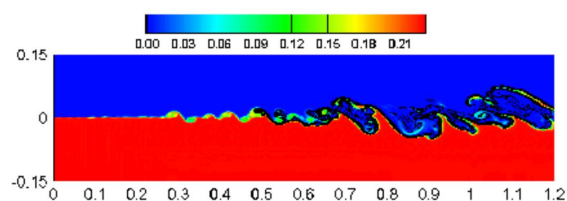
(a) mass fraction of O_2
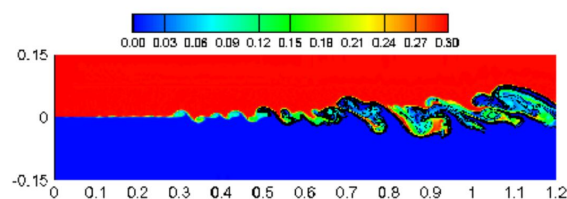
(b) mass fraction of H_2
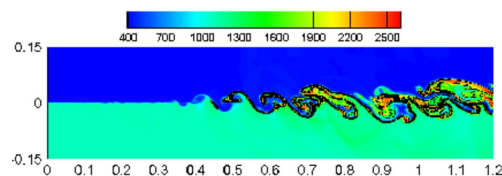
(c) temperature

FIGURE 12. Numerical results of supersonic combustion in mixing layers (iso-lines represent mass fraction of H_2O).

It was preliminarily found that the ILES can be applicable in computation of turbulent combustion, while high-resolution DNS and comparative analysis yet to be done. The reaction rate model in ILES has not well been resolved, which will be continually done in the future, though a supersonic combustion case was realized in the mixing layer flows.

References

[1] CHEN, S., XIA, Z., PEI, S., WANG, J., YANG, Y., AND XIAO, Z. (2012). Eddy viscosities in implicit large eddy simulations of decaying high Reynolds number turbulence with and without rotation. *Journal of Fluid Mechanics*, **703**(1), 1–28.

[2] FRANZELLI, B., RIBER, E., GICQUEL, L. Y., AND POINSOT, T. (2012). Large Eddy Simulation of combustion instabilities in a lean partially premixed swirled flame. *Combustion and flame*, **159**(2), 621–637.

[3] AKSELVOLL, K., AND MOIN, P. (2014). Large eddy simulation of a backward facing step flow. *Engineering Turbulence Modelling and Experiments*, **2**, 303–313.

[4] GARNIER, E., MOSSI, M., SAGAUT, P., COMTE, P., AND DEVILLE, M. (1999). On the use of shock-capturing schemes for large-eddy simulation. *Journal of Computational Physics*, **153**(2), 273–311.

[5] GRINSTEIN, F. (2014). Implicit Large-Eddy Simulation of Transition and Turbulence Decay. *Bulletin of the American Physical Society*, **59**.

[6] WIART, C. C., HILLEWAERT, K., BRICTEUX, L., AND WINCKELMANS, G. (2015). Implicit LES of free and wall-bounded turbulent flows based on the discontinuous Galerkin/symmetric interior penalty method. *International Journal for Numerical Methods in Fluids*, **78**(6), 335–354.

[7] WACHTOR, A. J., GRINSTEIN, F. F., DEVORE, C. R., RISTORCELLI, J. R., AND MARGOLIN, L. G. (2013). Implicit large-eddy simulation of passive scalar mixing in statistically stationary isotropic turbulence. *Physics of Fluids (1994-present)*, **25**(2), 025101.

[8] JIANG, G. S., AND SHU, C. W. (1996). Efficient implementation of weighted ENO scheme. *J. Comput. Phys*, **126**, 202–228.

[9] REN, Y. X., AND ZHANG, H. (2003). A characteristic-wise hybrid compact-WENO scheme for solving hyperbolic conservation laws. *Journal of Computational Physics*, **192**(2), 365–386.

[10] HU, X. Y., WANG, B., AND ADAMS, N. A. (2012). A high-efficiency and low-dissipation hybrid weighted essentially non-oscillatory scheme. *arXiv preprint arXiv:1210.3544*.

[11] DRIKAKIS, D., HAHN, M., MOSEDALE, A., AND THORNBER, B. (2009). Large eddy simulation using high-resolution and high-order methods. *Philosophical Transactions of the Royal Society of London A: Mathematical, Physical and Engineering Sciences*, **367**(1899), 2985–2997.

[12] TAYLOR, G. I., AND GREEN, A. E. (1937). Mechanism of the production of small eddies from large ones. *Proceedings of the Royal Society of London. Series A, Mathematical and Physical Sciences*, **158**(895), 499–521.

[13] BRACHET, M. E. (1991). Direct simulation of three-dimensional turbulence in the Taylor-Green vortex. *Fluid Dynamics Research*, **8**(1), 1–8.

[14] SHU, C. W., DON, W. S., GOTTLIEB, D., SCHILLING, O., AND JAMESON, L. (2005). Numerical convergence study of nearly incompressible, inviscid Taylor-Green vortex flow. *Journal of Scientific Computing*, **24**(1), 1–27.

[15] COLIN, O., DUCROS, F., VEYNANTE, D., AND POINSOT, T. (2000). A thickened flame model for large eddy simulations of turbulent premixed combustion. *Physics of Fluids (1994-present)*, **12**(7), 1843–1863.

[16] GOEBEL, S. G., DUTTON, J. C., KRIER, H., AND RENIE, J. P. (1990). Mean and turbulent velocity measurements of supersonic mixing layers. *Experiments in Fluids*, **8**(5), 263–272.